Full Length Article

Suppression of the green emission, texturing, solute-atom diffusion and increased electron-phonon coupling induced by Ni in sol-gel ZnNiO thin films

Oscar Marin[a,*], Patricio Alastuey[b], Ezequiel Tosi[a], Joseba Orive[c], Edgar Mosquera[d], Guillermo Zampieri[e,f], Sergio Suárez[e,f], David Comedi[a,*], Mónica Tirado[b,*]

[a] *Nanoproject – LAFISO, Facultad de Ciencias Exactas y Tecnologías, Universidad Nacional de Tucumán, and INFINOA (CONICET-UNT), San Miguel de Tucumán, Argentina*
[b] *Nanoproject – LNPD, Facultad de Ciencias Exactas y Tecnología, Universidad Nacional de Tucumán, and INFINOA (CONICET-UNT), San Miguel de Tucumán, Argentina*
[c] *Laboratorio de Materiales Funcionales a Nanoescala, Departamento de Ingeniería Química, Biotecnología y Materiales, Facultad de Ciencias Físicas y Matemáticas, Universidad de Chile, Santiago, Chile*
[d] *Departamento de Física, Universidad del Valle, Cali, Colombia*
[e] *Consejo Nacional de Investigaciones Científicas y Técnicas (CONICET), Argentina*
[f] *Instituto Balseiro, Centro Atomico Bariloche, Bariloche, Argentina*

ARTICLE INFO

ABSTRACT

$Zn_{1-x}Ni_xO$ thin films (nominal x = 0, 0.01, 0.02, 0.04, 0.1 and 0.2) were synthesized on silicon substrates through a sol-gel/dip-coating technique. Samples were studied by X-ray diffraction, scanning electron microscopy, photoluminescence spectroscopy, Rutherford backscattering spectrometry and depth-profiling X-ray photoelectron spectroscopy. The results from X-ray diffraction show growth in the wurtzite crystal structure for all samples, with cubic NiO being detected as a secondary phase for x = 0.2. While for x = 0 (pure ZnO) no texture is present, for $0 \le x \le 0.1$ strong preferential crystallization along the c-axis is observed. A tendency for Ni diffusion towards the film/Si substrate interface was observed. The formation of substitutional $Zn_xNi_{1-x}O$ solid solution for $0.01 \le x \le 0.04$ is suggested by the results. Photoluminescence spectra exhibit strong near band edge UV emission and suppression of deep defect-related emission in the visible upon Ni^{+2} incorporation into the ZnO lattice. As in pure ZnO, the UV emission in ZnNiO at room temperature is dominated by the first two phonon replica of the excitonic emission, however the LO phonon energy ($\hbar\omega_{LO}$) is reduced by up to ~ 15 meV in the $0 \le x \le 0.04$ range. Due to this reduction of $\hbar\omega_{LO}$, the exciton-phonon coupling increases, in consistency with a corresponding expected increase of the Fröhlich coupling constant with decreasing $\hbar\omega_{LO}$.

1. Introduction

Nanostructured ZnO films are being intensively studied due to their important technological applications [1], including UV light sensors [2], transparent electrodes for solar cells [3] and chemical sensors [4]. In addition to being a wide band gap semiconductor (~ 3.37 eV), ZnO exhibits an exciton binding energy of 60 meV, i.e. much larger than typical thermal energies at normal LED and laser operation temperatures, thus enabling robust excitonic emission [5,6]. The doping of ZnO with transition metals or the formation of stable solid solutions of ZnO and transition metal oxides are very attractive ways of engineering many physical properties of ZnO nanostructures [6–9]. In particular, the incorporation of Ni^{+2} into the ZnO lattice has been subject of great

attention, due to the magnetic properties of Ni^{+2} [8–11], which constitute the basis of emerging diluted magnetic semiconductors (DMS) that combine ferromagnetism at room temperature and optical transparency [12]. In addition, the introduction of Ni into ZnO can potentially be used as a way of tuning the photoluminescence and the electrical conductivity [13,14]. The incorporation of d- and f- transition metals into ZnO has been reported to lead to the quenching of the defect photoluminescence band in the visible [15], while both narrowing [14] and widening [16] of the ZnO band gap have been reported to occur due to Ni^{+2} incorporation.

However, the study of $Zn_{1-x}Ni_xO$ is particularly challenging, principally due to two factors: (i) the specific properties obtained have been often determined by the employed impurity incorporation technique

---

rather than by the properties of the impurity itself [17]; and ii) the low Ni solubility limit and the tendency for phase segregation into NiO and ZnO, which have been serious drawbacks to achieve stable solid solutions for Ni contents above typically x ~ 0.05 [18,19].

In this work, we explore a facile sol-gel synthesis route to fabricate $Zn_{1-x}Ni_xO$ films with nominal x = 0, 0.01, 0.02, 0.04, 0.1, 0.2 on Si substrate. Our study demonstrates that the incorporation of Ni^{+2} in the ZnO lattice produces important changes in the resulting microstructure and optical properties of the films for x < 0.2. Our analysis of the UV photoluminescence bands reveals an increase of the electron-phonon coupling with increasing Ni content, which results from a strengthened Fröhlich interaction associated with a Ni-induced reduction of the ZnO longitudinal optical phonon frequencies. In addition, we detect a tendency for Ni atom diffusion towards and Ni-rich phases formation at the film/Si substrate interface.

2. Materials and methods

The $Zn_{1-x}Ni_xO$ samples were synthesized by a sol-gel/dip-coating technique. The sol precursors were prepared from zinc acetate dehydrate (Aldrich, $Zn(C_2H_3O_2)_2 \cdot 2H_2O$) and nickel chloride hexahydrate (Cicarelli, $NiCl_2 \cdot 6H_2O$) with no further purification. An ethanolic solution of Zn^{+2} precursor was prepared and mixed with the adequate quantity of Ni^{+2} precursor to obtain solutions with a concentration of 0.3 M and $Zn^{+2}:Ni^{+2}$ in a proportion of 100:0 (x = 0) to 80:20 (x = 0.2) in atomic ratio. A volume of 1 ml of diethanolamine (DEA) (Aldrich, $C_4H_{11}NO_2$) was added to obtain a sol with a ~1:1 M ratio of $(Zn^{+2} + Ni^{+2})/DEA$ under constant stirring. After that, the solution was heated to 65 °C for 2 h. Finally, it was cooled down to RT. The sol was then aged for 24 h.

The sol was deposited on (1 1 1) oriented crystalline Si substrates (Ted Pella, Inc.) by 4 dip-coating/drying cycles at 5 cm/min and dried in an oven at 300 °C for 10 min. After deposition, the samples were annealed in a horizontal tube furnace at 600 °C for 1 h under a flow of 125 sccm of Ar (99.999% purity) and 30 sccm of O_2 (99.999% purity).

The samples compositions were studied by Rutherford backscattering spectrometry (RBS) with 2 MeV He^+ at a scattering angle of 165°, combined with Monte-Carlo simulations with SIMNRA© software to fit the obtained spectra. Composition depth-profiling was performed combining ion bombardment with X-ray photoelectron spectroscopy (DP-XPS). 1 keV Ar^+ ions (10 μA/cm^2) incident at 45° were used for the sputtering; photoelectrons were excited with monochromatic Al-K_alpha radiation (1486.71 eV) and energy-analyzed with a hemisphrical electron energy analyzer Phoibos 150 (SPECS). The crystalline structure and texture of the films were determined by X-ray diffraction (XRD) using a Bruker D8 Advanced diffractometer and a Cu Kα radiation source. The morphology of the samples was studied by scanning electron microscopy (SEM) using a ZEISS-GEMINI® SUPRA40 model microscope. Finally, photoluminescence (PL) spectra were determined at room temperature and atmospheric air using the 15 mW λ = 325 nm line of a Kimmon He-Cd laser as the excitation source and a Avantes compact CCD spectrometer for detection.

3. Results

3.1. Ni incorporation and distribution within the ZnNiO films

The RBS spectra show signals due to Zn, Ni, O and Si. A typical spectrum for $Zn_{1-x}Ni_xO$ with nominal x = 0.1 is shown in Fig. 1. From the fit of the spectra using SIMNRA© software, it is possible to determine the relative concentrations of Zn and Ni. For nominal x = 0.01 and 0.02 the Ni peak intensity is much lower and comparable to the statistical noise in our measurement conditions. For nominal x = 0.04, a single $Zn_{1-x}Ni_xO$ layer was enough to satisfactorily fit the RBS spectra within the statistical uncertainty. For the samples with x = 0.1 and 0.2, in turn, no successful fit was possible with a single layer model.
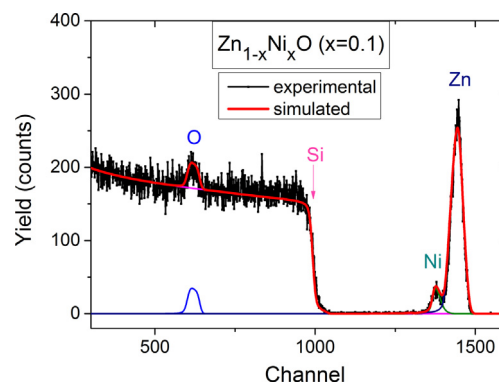

Fig. 1. Typical RBS spectrum obtained from the $Zn_{1-x}Ni_xO$ sample with x = 0.1. The simulation fit using a multilayer model is also shown.

As shown in Fig. 2(a) and (c) in the spectrum region for Zn and Ni, the experimental Ni peaks are shifted towards lower channel numbers (i.e. lower scattered He^+ energies) with respect to the calculated peak positions for a single layer with uniform Ni concentration. This shows that the Ni is depleted from the surface region and accumulated close to the film/substrate interface, where the backscattering He^+ arrive with energies lower than those backscattered from the film surface, Hence, for x = 0.1 and 0.2, a multilayer model was needed to fit the spectra, as shown in Fig. 2(b) and (d).

In Table 1, the x values determined from the SIMNRA© simulation fits for each layer are shown. For nominal x = 0.1 and x = 0.2, the surface layers are indeed Ni-poor while the film/substrate interface layers are Ni-rich. For the x = 0.1 sample an additional intermediate layer had to be assumed in the fit, which was not necessary for x = 0.2. Note that in spite of the important change in x with film depth, the thickness-weighted averaged x values turn out to be close to the nominal ones, stressing the fact that Ni atoms have redistributed at some stage during the film fabrication towards the substrate. The total film thicknesses as determined from the SIMNRA© simulations range between 46 and 58 nm, which are in close agreement with cross section SEM determined thicknesses.

The non-homogeneous Ni distributions within the ZnNiO films as deduced from the RBS analysis were confirmed by DP-XPS on two selected samples (nominal x = 0.02 and 0.2). The XPS spectra for the $Zn2p_{3/2}$, O1s, $Ni2p_{3/2}$, Si2s and Zn3s photoelectron peaks are shown in Fig. 3 for x = 0.02 and in Fig. 4 for x = 0.2, at various Ar^+ sputtering stages. The $Ni2p_{3/2}$ peak intensities for x = 0.02 [Fig. 3d] are much lower than for the x = 0.2 sample [Fig. 3d], reflecting the factor of 10 ratio in nominal Ni concentration between both samples. In both Figs. 3 and 4, the spectra highlighted in green, blue, and black correspond to, respectively, the initial, intermediate, and final stages of the depth profiling. The spectra in Fig. 3(a) and 4(a) show that, initially, only the peak from the film (Zn3s) is seen, while later both peaks have comparable intensities and, as the sputtering process resumes, the spectra become dominated by the peak from the substrate (Si2s).

Figs. 3(b, c) and 4(b, c) show that the $Zn2p_{3/2}$ and O1s peaks initially remain nearly constant and then decrease monotonically. In contrast, Figs. 3(d) and 4(d) show that the evolution of the $Ni2p_{3/2}$ peaks is very different. Particularly in Fig. 4(d), one can notice that: (i) the peak at an intermediate sputtering time is more intense than at the beginning, (ii) at the end of the sputtering, when the O and Zn peaks have decreased to very low intensities, the $Ni2p_{3/2}$ peak has still considerable intensity, and iii) the $Ni2p_{3/2}$ peak shape changes as the sputtering proceeds deeper into the film.

All peaks in Figs. 3 and 4, except those for the $Ni2p_{3/2}$, were fitted with a combination of a single Voigt function and a linear background. The $Ni2p_{3/2}$ spectra demanded a special analysis; reasonable fits of the corresponding peaks were achieved using three components, as shown in Fig. 5, labeled as Ni1, Ni2 and Ni3. The Ni1 component, which
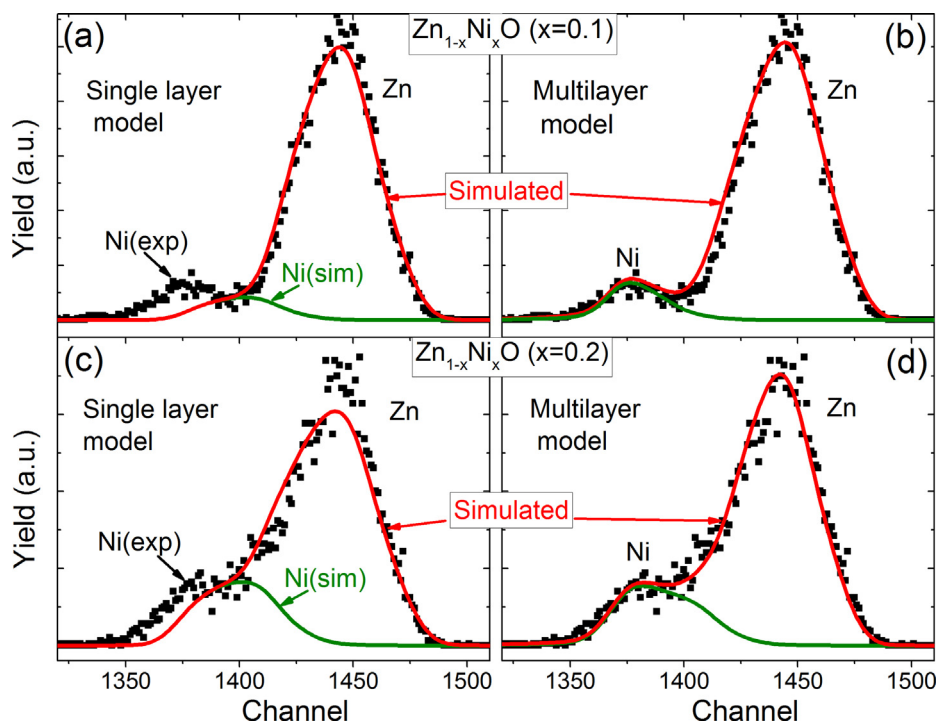
Fig. 2. Details of the SIMNRA© simulation fits using a single layer model (a and c) and a multilayer model (b and d) of the experimental RBS data in the region of the Zn and Ni peaks for $Zn_{1-x}Ni_xO$ films with x = 0.1 (a and b) and x = 0.2 (c and d).

Table 1

Nominal x values in $Zn_{1-x}Ni_xO$ films and corresponding values as-deduced from SIMNRA© fits of RBS spectra. For x = 0.1 and x = 0.2, more than one layer had to be assumed in the model to satisfactorily fit the experimental data. The corresponding layer thicknesses (t_{RBS}), and the weighted average $\langle x_{RBS}\rangle$ are also shown.

Nominal x	x (surface layer 1)		x (intermediate layer 2)		x (film/substrate interface layer 3)		$\langle x_{RBS}\rangle$
	x_{RBS}	t_{RBS} (nm)	x_{RBS}	t_{RBS} (nm)	x_{RBS}	t_{RBS} (nm)	
0.01	~0.01	58	–	–	–	–	–
0.02	~0.02	52	–	–	–	–	–
0.04	0.05	46	–	–	–	–	–
0.1	0.00	30	0.07	23	0.67	5	0.09
0.2	0.13	36	–	–	0.52	18	0.26

dominates in the first sputtering stages, resembles the spectrum of NiO. The Ni3 component was determined by fitting a $Ni2p_{3/2}$ spectrum measured on a clean metallic Ni sample. These two components are, therefore, assigned to oxidized and metallic Ni, respectively. The interpretation of the intermediate Ni2 component requires some further analysis.

The overall situation that emerges from the DP-XPS experiment is summarized in Fig. 6(a) and (b), where the integrated peak intensities are plotted against the sputtering time [20]. The peaked behavior of the Ni intensities for the two samples is in agreement with the formation of a positive Ni gradient towards the film/substrate interface, as previously deduced from the RBS measurements for x = 0.1 and 0.2. Remarkably, for x = 0.2, the $Ni2p_{3/2}$ integrated intensity becomes even larger than those for Zn and O for long sputtering times [Fig. 6b], indicating that some Ni has diffused into the substrate.

The evolution of the Ni1, Ni2, Ni3 components intensities, shown in Fig. 6(c) and (d), allows grasping further details on this process. The Ni1 component dominates the spectra at shallow depths, and is responsible for the Ni depletion profile observed in that region in Fig. 6(a) and (b). This component, assigned to oxidized Ni, could be associated to

both substitutional Ni within the ZnO lattice or a NiO phase. It is interesting to compare the behavior of Ni1 with the O1s "excess" as defined by the difference between the O1s and $Zn2p_{3/2}$ integrated intensities shown in Fig. 6(b) for x = 0.2. This is done in Fig. 7(a). It is clear that there is a close correlation between the evolutions of the O1s "excess" and the Ni1 component, giving further evidence that the latter originates from Ni atoms bonded to O.

The Ni2 component, in turn, is initially very weak; however it increases and becomes the dominant contribution close to the film/substrate interface [see Fig. 6c and d]. It may be noted that this increase occurs together with that of the Si2s peak [Fig. 6a and b]. This is more clearly shown in Fig. 7(b), where the evolutions of the Ni2 and Si2s integrated intensities for the $Zn_{1-x}Ni_xO$ sample with x = 0.2 are plotted together. The close agreement between both data sets strongly suggests that the Ni2 component is due to Ni atoms bound to Si atoms of the substrate.

Finally, the component Ni3, ascribed to metallic Ni, remains always as a minor contribution. We note, however, that being a component much narrower than the other two it is more subject to errors caused by the noise in the spectra.

3.2. Film structure and morphology

The obtained XRD patterns for the $Zn_{1-x}Ni_xO$ samples are shown in Fig. 8(a). For x = 0 (i.e., pure ZnO), multiple reflections, corresponding to (1 0 0), (0 0 2), (1 0 1) and (1 0 3) lattice planes of the hexagonal ZnO wurtzite structure, are observed. Interestingly, the pattern changes quite abruptly as Ni is incorporated to the lattice. For x as low as 0.01, strong preferential orientation along the c-axis is evidenced, which is also observed for x = 0.02, 0.04 and 0.1. For x = 0.2, this preferential orientation disappears, and multiple reflections corresponding to the ZnO wurtzite phase are again observed. In addition, the cubic NiO is also revealed as a second phase, as evidenced by its (1 1 1), (2 0 0) and (2 2 0) Bragg reflections.

The degree of preferred orientation of the films was determined by calculating the texture coefficient (TC_{hkl}) for the (0 0 2) reflection of the
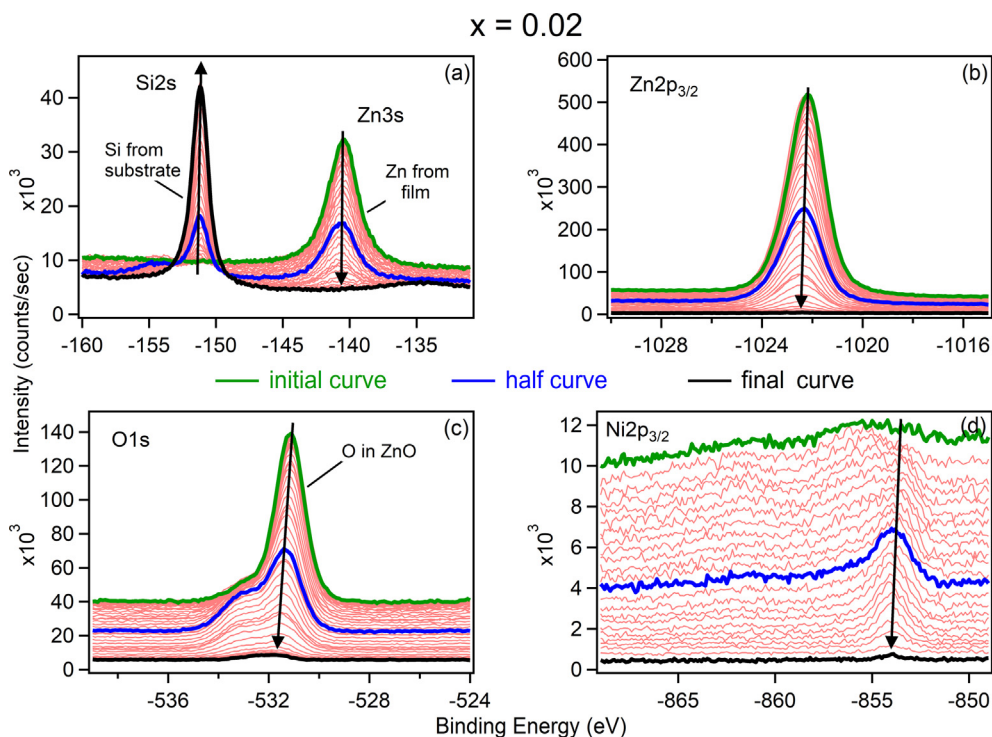
x = 0.02

Fig. 3. XPS spectra measured after various sputtering stages in the region of (a) Si2s and Zn3s, (b) Zn2p$_{3/2}$, (c) O1s, and (d) Ni2p$_{3/2}$, for Zn$_{1-x}$Ni$_x$O samples with nominal x = 0.02. Spectra are conveniently shifted vertically to avoid overlap for clarity. Arrows indicate evolution with increasing sputtering time.

wurtzite structure, using the relation [21]:

$$TC_{(002)} = \frac{I_{(002)}/I_{0,(002)}}{(1/N)\sum I_{(hkl)}/I_{0,(hkl)}}, \qquad (1)$$

where $I_{(hkl)}$ is the measured intensity, $I_{0,(hkl)}$ is the reference intensity according to JCPDS 036-1451 card, and N is the total number of

observed reflections. The results are shown in Fig. 8(b). It should be noted that high TC values mean high degree of preferential (0 0 2) orientation. As observed in Fig. 8(b), while pure ZnO hardly exhibits any texture (i.e. TC ≈ 0), for x = 0.01 TC increases abruptly and remains high (although it decreases slightly) up to x = 0.04. In the sol-gel technique, several parameters affect the growth and orientation of
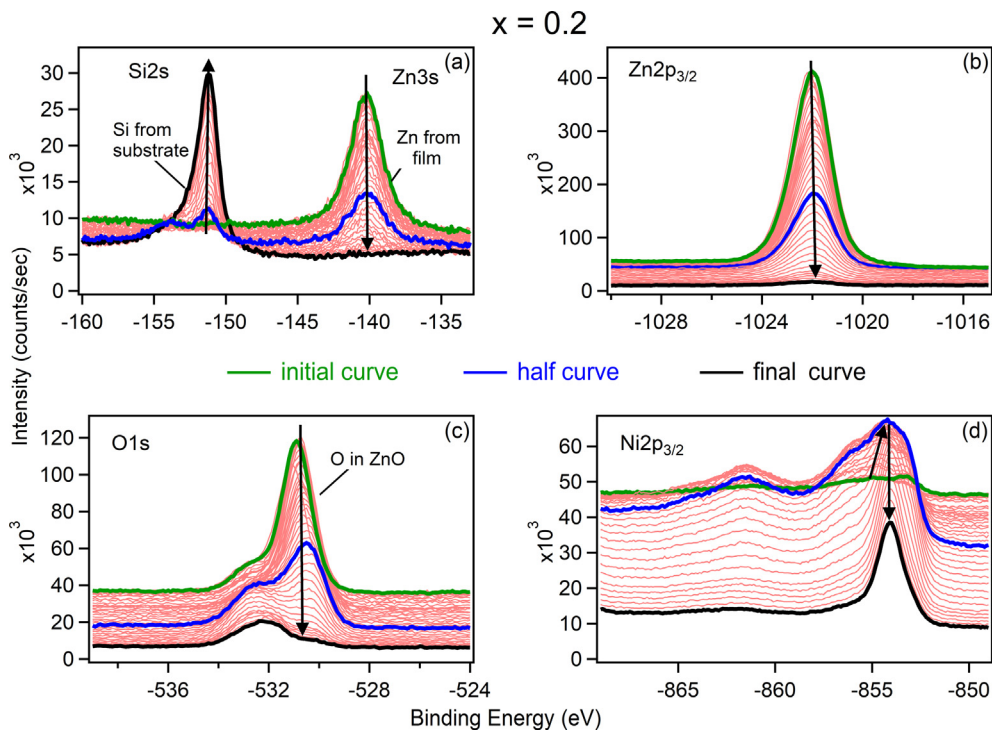
x = 0.2

Fig. 4. XPS spectra measured after various sputtering stages in the region of (a) Si2s and Zn3s, (b) Zn2p$_{3/2}$, (c) O1s, and (d) Ni2p$_{3/2}$, for Zn$_{1-x}$Ni$_x$O samples with nominal x = 0. 2. Spectra are conveniently shifted vertically to avoid overlap for clarity. Arrows indicate evolution with increasing sputtering time.
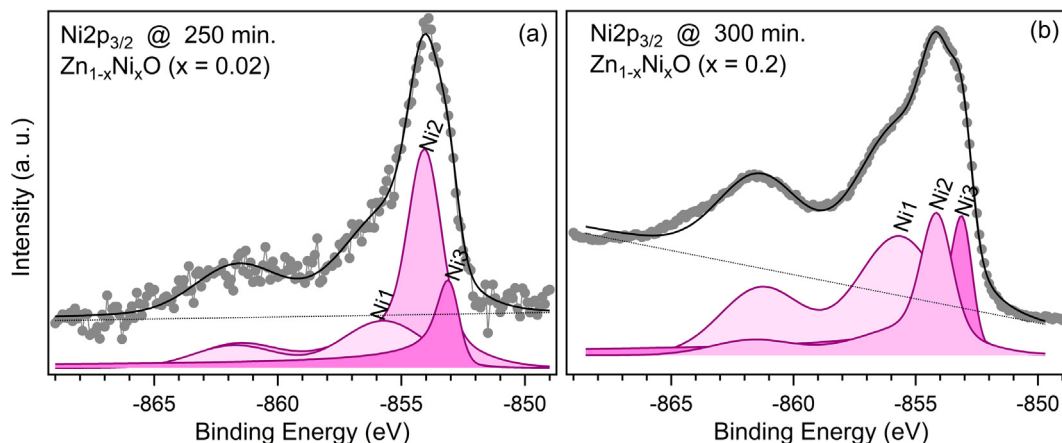
Fig. 5. XPS spectra showing the $Ni2p_{3/2}$ peak for $Zn_{1-x}Ni_xO$ with (a) x = 0.02 (after 250 min sputtering) and (b) x = 0.2 (after 300 min sputtering). The fit curves and their main components, Ni1, Ni2 and Ni3, are also shown.

synthesized films, including type of chelating agent, valence of metallic ions and drying temperature [22,23].

The *c* parameter was refined from the XRD data with the pattern matching mode (Le Bail refinement) using the FullProf software [24], see Fig. 8(c). Since the data for x = 0.2 is noisy and there are two phases, the refinement could not be carried out for this sample. As can been seen, the *c* parameter for the pure ZnO sample (*c* = 5.2117 Å) is strongly reduced for x = 0.01 (*c* = 5.1984 Å). Further increase in x leads to an increase in c. Hence, the XRD analysis shows that Ni incorporation leads too strong changes for even x = 0.01. For samples with x between 0.01 and 0.1, the detection of one phase only (i.e. wurtzite ZnO) in Fig. 8(a) indicates that Ni is being mainly incorporated substitutionally into the ZnO lattice. For x = 0.2, the presence of the cubic phase of NiO shows that a considerable amount of Ni is not substitutional in the ZnO lattice but is incorporated within NiO regions in the film.

Fig. 9 shows SEM images for samples with x = 0, 0.02, 0.04, 0.1 and 0.2. The films are composed by grains with broad size dispersion in the nanoscale range. The mean grain sizes as determined from the SEM images are shown in Fig. 9(f); it shows that the mean grain size increases drastically by slightly less than a factor of two when going from x = 0 to x = 0.01, and then decreases gradually with increasing x. Also noticed in Fig. 9(a–d) is a more compact grain packing in the Ni-containing materials as compared to pure ZnO.

It is interesting to note that the x-dependence of the mean grain size [Fig. 9f] is qualitatively similar to that exhibited by the texture coefficient in Fig. 8(b). This fact emphasizes the consistency between the different experimental data (XRD and SEM) in revealing the strong impact of relatively small amount of Ni (x = 0.01) on the resulting structural characteristics of the films; an impact that is gradually reduced as x increases further.
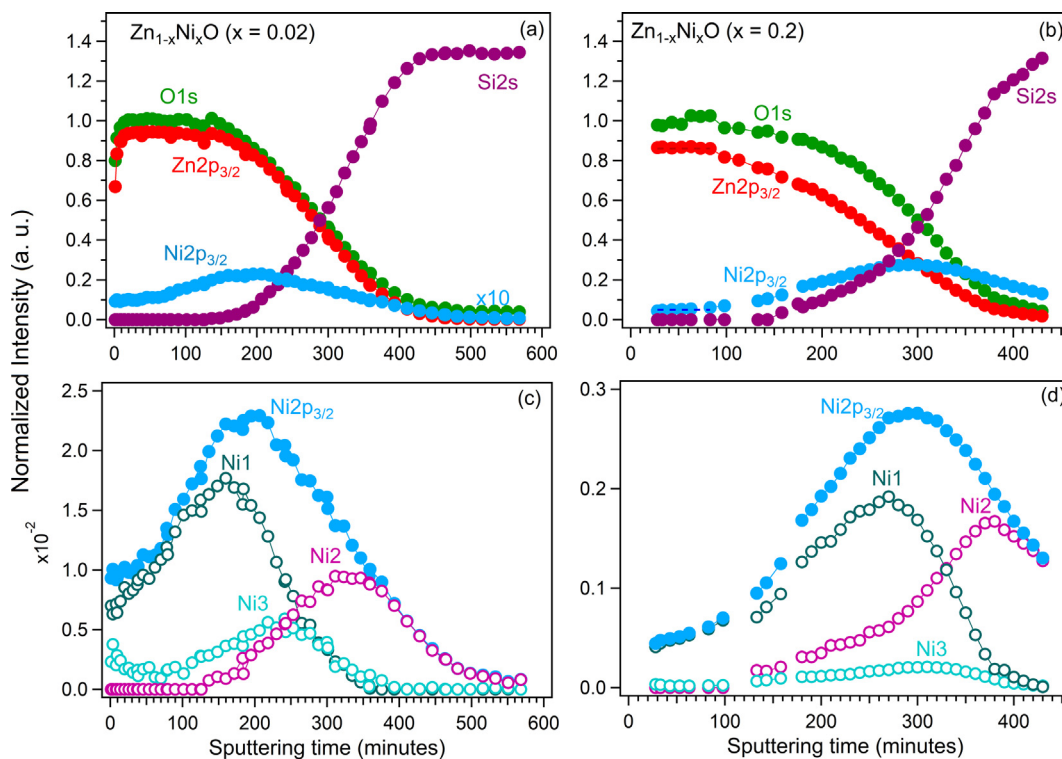

Fig. 6. Photoelectron peak intensities and the relative contributions from the three $Ni2p_{3/2}$ (Ni1, Ni2, Ni3) components as functions of the Ar^+ sputtering time for $Zn_{1-x}Ni_xO$ with x = 0.02 (a and c) and x = 0.2 (b and d). The $Ni2p_{3/2}$ intensities for the x = 0.02 sample in (a) are multiplied by 10.
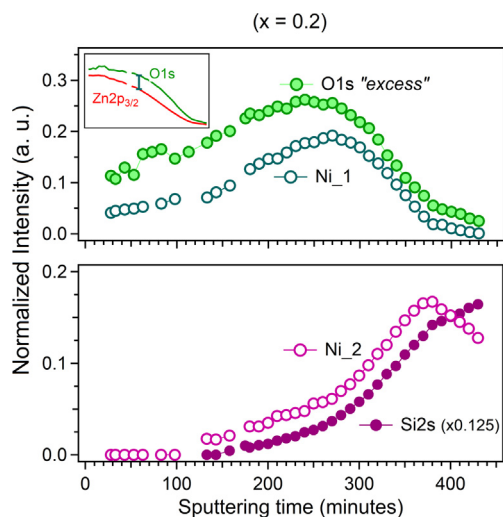
Fig. 7. (a) O1s "excess", as defined by the intensity difference between the O1s and Zn2p$_{3/2}$ photoelectron peaks (see insert) taken from Fig. 6(b); and (b) the Ni2 component and Si2s peak intensities taken from Fig. 6(d) and (b), respectively, as functions of the sputtering time.
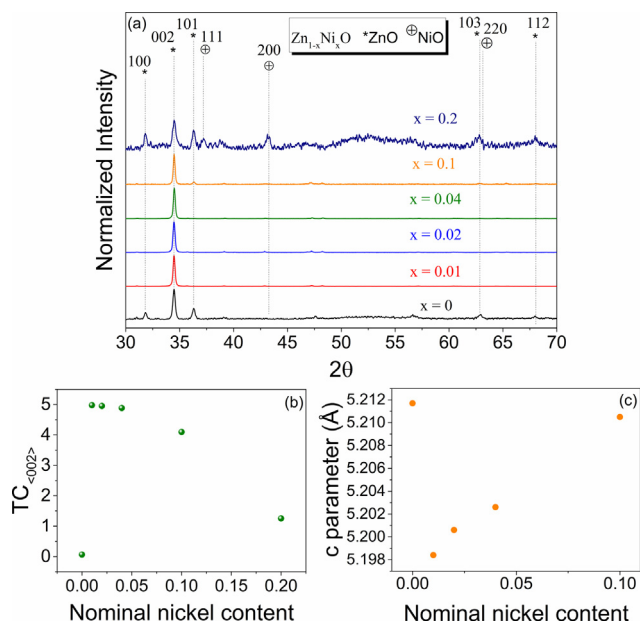

Fig. 8. (a) XRD patterns of Zn$_{1-x}$Ni$_x$O thin films; (b) texture coefficient analysis for the wurtzite (0 0 2) lattice plane; (c) c parameter obtained from Pattern Matching refinement (FullProf Software).

3.3. Photoluminescence

Fig. 10(a) shows the normalized PL spectra for the Zn$_{1-x}$Ni$_x$O samples. The normalization of the spectra was carried out by dividing the emission intensity values in each spectrum by the corresponding maximum intensity (which in all cases was equal to the maximum of the UV band). The UV emission due to excitonic or near band edge transitions in ZnO dominates all spectra. The decreasing signal-to-noise ratio shows that the overall PL intensities decrease with increasing x. However, this intensity reduction is more important for the emission in the visible, as clearly observed in Fig. 10(a) (note the almost complete suppression of the band in the visible for x = 0.04 and 0.1) and in Fig. 10(b), which shows a steep increase of the PL intensity ratio, I$_{UV}$/I$_{VIS}$, from x = 0 up to x = 0.1. In contrast, for the sample with x = 0.2, a relative increase of the emission in the visible with respect to the UV

emission is observed.

Fig. 11 shows the UV part of the PL spectra from all the Zn$_{1-x}$Ni$_x$O samples. It is clear that the peak blueshifts significantly when going from x = 0 to x = 0.01. However, for larger x values, the low wavelength side of the peak remains nearly unchanged, while the high wavelength side is reduced with increasing x. As previously reported for sol-gel [23] and vapor transport [25,26] synthetized ZnO, the UV emission at room temperature can be decomposed into two components, which are attributed to the excitonic emission (FX) first- and second-order longitudinal optical phonon replica (FX-1LO and FX-2LO). In this work, we have applied a similar fit analysis for the UV emissions from all the ZnNiO samples to determine the position and intensities of both components. Typical double-Voigt function fits to the energy PL spectra are shown in Fig. 12(a) and (b).

Fig. 12(c) shows the FX-1LO and FX-2LO components peak positions as functions of the nominal x. For the case of pure ZnO films (x = 0), the energy difference is 76 meV, in consistency with previous studies in ZnO [23,25,26]. For x = 0.01, both components are blueshifted by few meV. For larger x the blueshift continues but eventually the FX-1LO component peak position saturates while the FX-2LO blueshifts a few meV more. As a result, the energy difference between both positions decreases to about 60 meV for x = 0.04 and remains nearly unchanged for larger x. Fig. 12(d) shows the ratio of the integrated intensities of the two components, A_{FX-2LO}/A_{FX-1LO}, as a function of x. As can be seen, this ratio increases with x, reaches a maximum for x = 0.1 and then decreases for x = 0.2.

4. Discussion

The RBS and DP-XPS work done here clearly shows that Ni atoms tend to diffuse towards the Si substrate during the fabrication of the films. While the Ni diffusivity in solid ZnO is very low [27], Ni diffusion can be orders of magnitude larger in the intermediate stages between the sol and the final solid film. Hence, some of this diffusion may have occurred through the liquid state that partially characterizes the gel. In our fabrication technique, a layer-by-layer dip coating deposition of the sol on the Si substrate was carried out. Each dip-coating deposition of the sol was followed by a drying step at 300 °C. In addition, as usual in sol-gel synthesis, the aerogel, polymeric-like film obtained after the final drying was annealed for 1 h at 600 °C until it was fully converted into a compact, solid ZnNiO film. During this transformation, in which remaining solvent molecules are eliminated through a porous, albeit densifying network, there could be additional enhanced Ni diffusion away from the film to the Si substrate. Recently [28], it has been shown that Ni diffusivity through interstitial Ni sites in crystalline Si is large even at room temperature. Interstitial Ni in Si may destabilize the Si-Si bonds and favor the formation of Ni silicides at low temperatures as well [29]. Hence, the Si substrate probably acts as an efficient sink for Ni atoms, providing the driving force that triggers the observed Ni diffusion towards the Si substrate.

The XRD data, in turn, show that small additions of the Ni precursor strongly affect the growth processes during the synthesis and the final crystal orientation; this effect is more marked for low Ni concentration and gradually diminishes as x increases [Fig. 8b, c and f]. Part of this effect may be due to intrinsic bonding differences between the Ni^{+2} and Zn^{+2}. For instance, the lower Ni^{+2} ionic radius (0.069 nm) than that of Zn^{+2} (0.074 nm) [30] (i.e, a difference of 6.7%) may easily account for a reduction of the c lattice parameter by 0.27% as observed for x = 0.01 as compared to pure ZnO [Fig. 8c] due to Ni^{+2} substitution within the ZnO lattice. Indeed, despite the Ni induced changes in lattice parameter and preferred orientation, the overall crystalline symmetry does not change and remains hexagonal wurtzite for x = 0.01, 0.02, 0.04 and 0.1 [Fig. 8a]. The XPS spectra, in turn, show that most of the Ni atoms are in the Ni^{+2} (oxidized) state [Fig. 6c]. The formation of stable solid solutions of Zn$_{1-x}$Ni$_x$O for x below ~0.04 is in agreement with trends already reported in the literature [14].
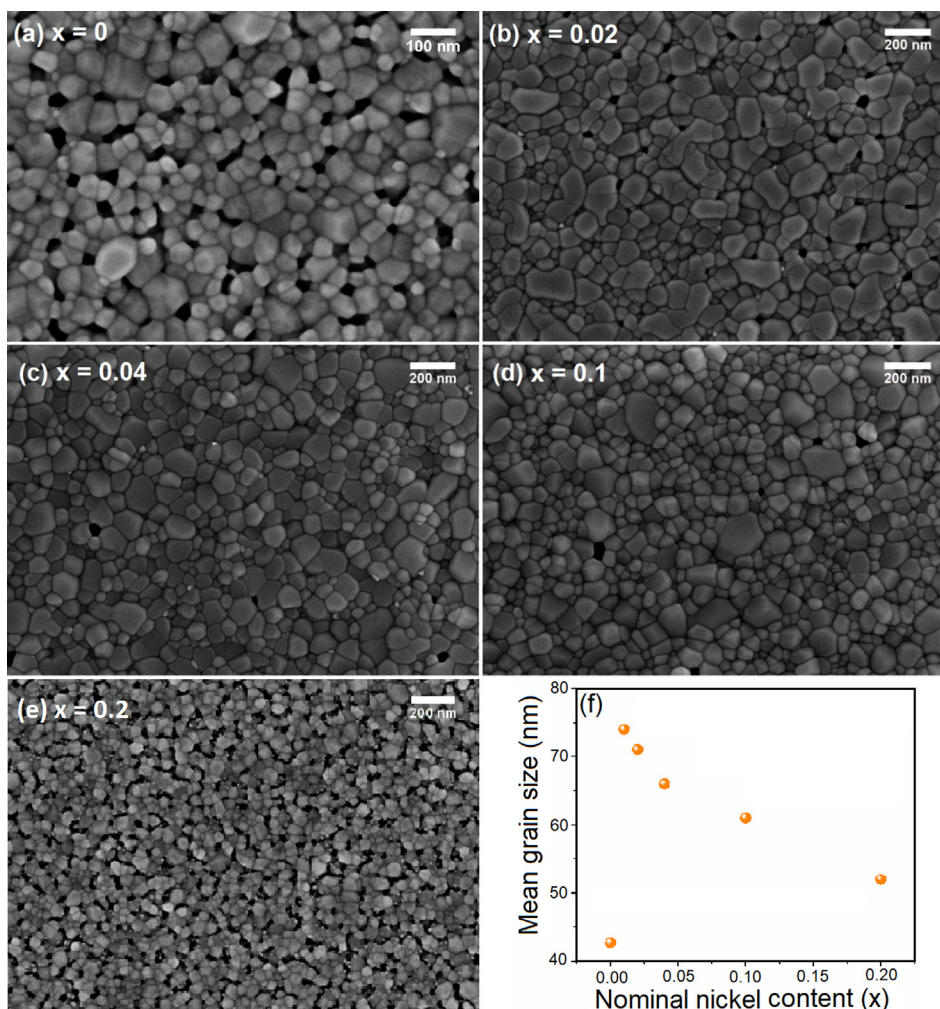
Fig. 9. (a–e) SEM micrographs of $Zn_{1-x}Ni_xO$ thin films, (f) mean grain size measured from SEM micrographs.

However, the increment of the *c* parameter for x > 0.01 suggests that as the Ni content increases, some Ni atoms may not be incorporated substitutionally. For x = 0.2, the XRD data show the presence of a NiO cubic phase [Fig. 8a], as can be expected since this corresponds to a Ni concentration well above the solubility limit of Ni in ZnO. The RBS and DP-XPS data, in turn, reveal that the NiO regions may not be evenly distributed across the film but located close to the substrate. Both, the DP-XPS and RBS data give evidence for the formation of a Ni-rich layer close to the substrate and a Ni poorer region close to the film's surface (see Table 1 and Figs. 6 and 7). Therefore, and since the wurtzite structure is expected to be destabilized for large x, it is reasonable to assume that the NiO phases preferentially formed in the Ni rich region, while the observed wurtzite phase predominates in the Ni poor region with the Ni substitutionally incorporated in $Zn_xNi_{1-x}O$.

Texturing during ZnO sol-gel synthesis is known to be favored when nucleation initiates at the gel-substrate interface (heterogeneous nucleation), and inhibited when the nucleation of crystallites occurs away from the sol-substrate interface (homogenous nucleation) [31]. The latter seems to be the case for pure ZnO, which shows no texture. The drastic change in nucleation mode for x = 0.01, whose signature is a strong texture [Fig. 8b] and large crystallites [Fig. 9f] suggests that the Ni precursors activate the formation of heterogeneous nucleation centers at the gel-substrate interface, promoting the growth of c-axis oriented wurtzite $Zn_{1-x}Ni_xO$ crystallites. However, as the Ni concentration is increased, the wurtzite structure is destabilized by the competing formation of highly Ni-rich regions at the film/substrate interface (as revealed by RBS, Table 1, and by DP-XPS), which, as observed in

Fig. 8(b) and 9, results in decreasing texturing degree and mean grain size with increasing x. Eventually, this process ends up leading to the formation of cubic NiO crystallites, as deduced from the XRD data for x = 0.2 [Fig. 8a].

As for the PL data, there are three main effects: (1) The overall PL intensity decreases; (2) the emission in the visible decreases more strongly and is eventually suppressed, as evidenced by the spectra in Fig. 10(a) and the I_{UV}/I_{VIS} ratio increases with x in Fig. 10(b); (3) the PL band in the UV blueshifts when going from x = 0 to x = 0.01 and shows significant shape changes with increasing x (Figs. 11 and 12). The incorporation of Ni^{+2} into the ZnO lattice can explain effect (1), considering the formation of non-radiative recombination centers (NRC), which are usually induced by transition metals in ZnO [32]. Effect (2) is probably related to a competition between the crystallite size increase induced by the Ni [Fig. 9f] which is expected to reduce the effective deep defect density associated with the grain boundaries, and the increasing number of NRC induced by Ni incorporation, which also competes with the deep defect transitions that give rise to the emission in the visible. The decrease of I_{UV}/I_{VIS} ratio for the sample with x = 0.2 is clearly related to the formation of NiO phase inclusions at the expense of the wurtzite ZnO-related phase, which results in a reduction of the ZnO-related excitonic emission and an increase in wurtzite ZnNiO/cubic NiO interface-related defect emissions.

Regarding the changes in the UV emission [effect (3), Figs. 11 and 12], it is fairly established that at room temperature, for ZnO, the UV PL is in general dominated by the first two phonon replicas of the exciton emission (FX-1LO and FX-2LO) [23,25,26]. The FX-nLO replicas are
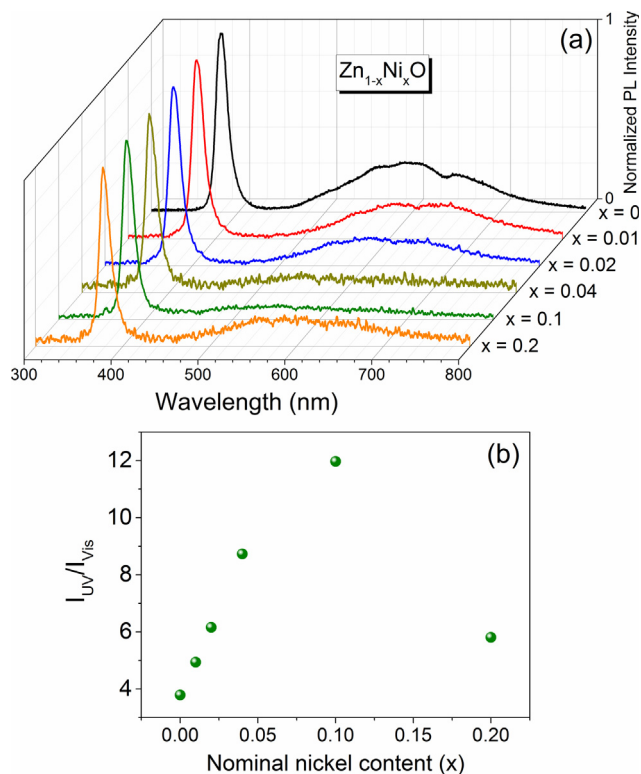
Fig. 10. (a) PL spectra from $Zn_{1-x}Ni_xO$ samples (b) UV to visible PL intensity ratio (I_{UV}/I_{VIS}) as a function of the nominal Ni content.
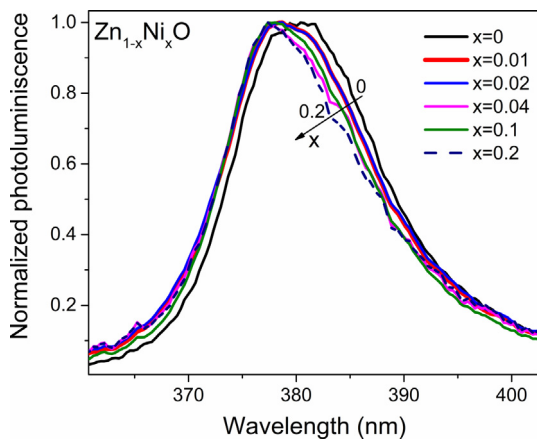

Fig. 11. PL spectra from the $Zn_{1-x}Ni_xO$ samples in the UV region.

centered at energies given by the following expression:

$$E_{FX-nLO} = E_{FX} - n\hbar w_{LO} + \langle E_k \rangle, \qquad (2)$$

where E_{FX} is the photon energy of the FX emission, n = 1, 2… are integer numbers that indicate the replica orders, $\hbar\omega_{LO}$ is the energy of the longitudinal optical phonon in ZnO and $\langle E_k \rangle$ is the exciton mean kinetic energy [26]. Hence, the blueshifts observed in Fig. 13(c) for both FX-1LO and FX-2LO components (up to ~15 meV and ~30 meV, respectively) are not due to a Ni-induced bandgap widening [16] (which would affect both components equally), but due to a reduction of $\hbar\omega_{LO}$ with respect its value in ZnO by up to ~15 meV. Indeed, if one looks at the difference between the photon energies for the first and second phonon replica emissions ($\Delta E = E_{FX-2LO} - E_{FX-1LO}$), from Eq. (2) it is expected to be:

$$\Delta E = \hbar w_{LO} \qquad (3)$$

As shown in Fig. 12(c) and mentioned above, for x = 0, the energy difference between the UV emission components found from the fit is 76 meV, which as in previous reports [23,26] is in reasonable agreement with the expected value of $\hbar\omega_{LO}$ for ZnO. For the samples with low Ni concentrations [i.e for $0 < x \le 0.04$, see Fig. 12c], this value rapidly diminishes down to $\Delta E = \hbar\omega_{LO} \approx 60$ meV. A reduction of $\hbar\omega_{LO}$ in ZnNiO is consistent with an alloying effect expected and observed in cationic and anionic II-VI ternary compounds [33,34] and the fact that the LO phonon energy in NiO (≈ 19 meV, as deduced from optical studies [35]) is much lower than in ZnO. The x-dependence of ΔE in Fig. 12(c), however, is somewhat stronger than can be expected from a simple weighted average of the LO phonon energies of ZnO and NiO. Unfortunately, no direct measurements of the LO phonon frequency in ZnNiO films are yet available. Nevertheless, it is clear that in addition to a simple alloying effect, strains due to the lattice compression and local atomic relaxations around the substitutional Ni^{2+} ions could play an additional role, leading to bowing effects [33]. In this regard, it is interesting to consider the strong increase of the A_{FX-1LO}/A_{FX-2LO} ratio as seen in Fig. 12(d), which implies an increasing exciton-phonon coupling with increasing x. It is well-known that the exciton-phonon coupling in ZnO is dominated by the Fröhlich interaction [36] due to the effects of electric field that results from the polar lattice vibrations on the exciton's electron and hole. A measure of the electron-phonon Fröhlich interaction strength is the Fröhlich coupling constant [37]:

$$\alpha = \frac{e^2}{\hbar} \sqrt{\frac{m^*}{2\hbar\omega_{LO}}} \left(\frac{1}{\varepsilon_\infty} - \frac{1}{\varepsilon_0} \right), \qquad (4)$$

where e is the electron charge, $\hbar$ is Planck's constant over 2π, m^* is the electron effective mass, and ε_∞, ε_0 are the electronic and static dielectric constants, respectively. For substitutional Ni^{2+} in the Zn^{2+} sublattice of ZnO, which according to the RBS and XRD data is the case for $0 \le x \le 0.04$, one can expect little change of ε_∞, ε_0 and m^* with x, given that the dielectric constants of NiO and ZnO do not differ much [38,39] and the fact that the effective mass is dictated by the band structure close to the center of the Brillouin zone, which should be essentially determined by the ZnO bonding for low x. As for the third variable in Eq. (3), namely the LO phonon energy $\hbar\omega_{LO}$, our own data for ΔE in Fig. 12(c) indicate (considering Eq. (2) its important reduction with increasing x in the $0 \le x \le 0.04$ interval. According to Eq. (3), such a reduction of $\hbar\omega_{LO}$ should imply an increase of the Fröhlich coupling constant α as $(\hbar\omega_{LO})^{-1/2}$. Indeed, if we take the experimental values of the A_{FX-2LO}/A_{FX-1LO} ratio from Fig. 12(d) as an experimental measure of the electron-phonon interaction, and plot it against the experimental $(\Delta E)^{-1/2}$ values from Fig. 12(c), we obtain a close correlation (see Fig. 13) for samples within the $0 \le x \le 0.04$ region. Hence, it is possible to conclude that the interpretation above in terms of the electron-phonon Fröhlich interaction for substitutional $Zn_{1-x}Ni_xO$ is sound. The data for the samples with x = 0.1 and 0.2, in contrast, do not agree well with the above correlation and the reason for this could be related to the strong Ni segregation and phase separation detected in these samples, the activation of other electron-phonon mechanisms, interface effects or any combinations of these factors which are not taken into account in the simple analysis above.

5. Conclusions

$Zn_{1-x}Ni_xO$ thin films (nominal x within the $0 \le x \le 0.2$ interval) were synthesized on silicon substrates by a sol-gel/ dip-coating technique. The samples were analyzed by XRD, RBS, DP-XPS, PL and SEM. The following conclusions can be drawn:

(1) While pure ZnO film (x = 0) does not show preferential orientation, the incorporation of the Ni results in strong preferential orientation along the c-axis of wurtzite for $0.01 \le x \le 0.04$ and large crystallites. For x = 0.1 and 0.2 the preferential orientation and the
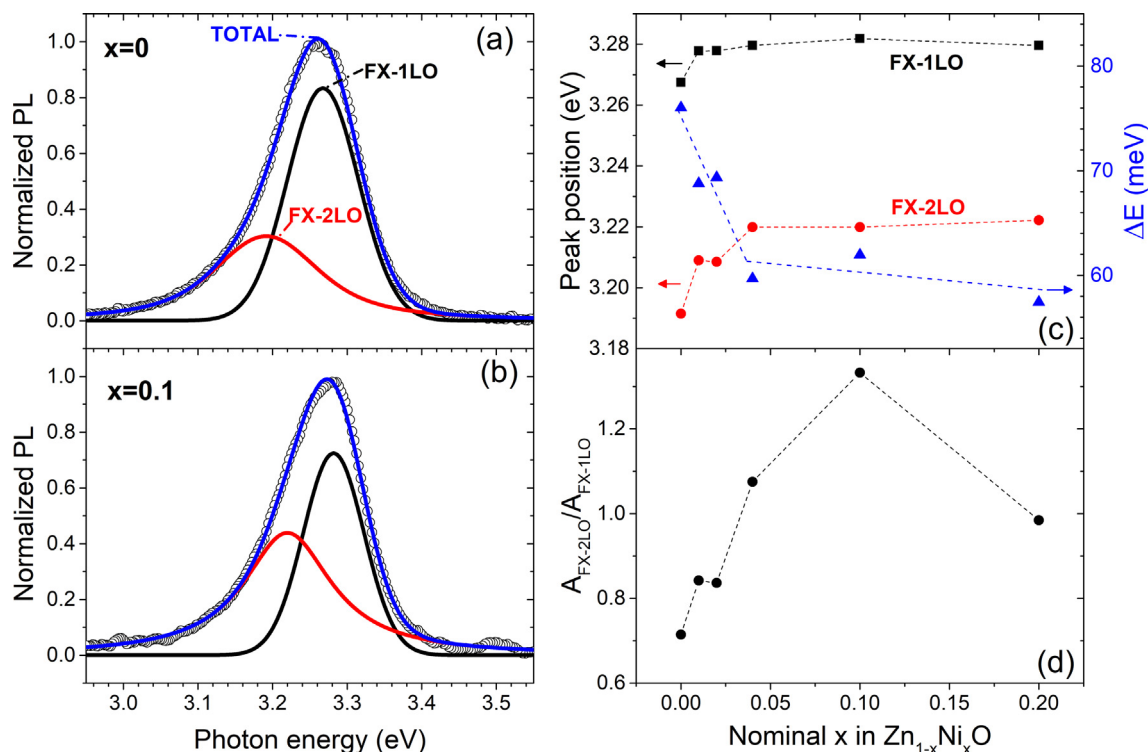
Fig. 12. (a) and (b) Typical double Voigt function fit for the UV emission from $Zn_{1-x}Ni_xO$ samples, shown for (a) pure ZnO (x = 0) and for (b) x = 0.1. Open circles: experimental data. Lines: total fit function (blue) with its FX-1LO (black) and FX-2LO (red) components. (c) Peak positions of the FX-1LO (black squares) and FX-2LO (red circles) components obtained from the fits, and the difference ΔE between them (blue triangles), as functions of the nominal x. (d) Ratio of integrated intensities of both components as function of the nominal x. Lines in (c) and (d) are guides for the eyes.
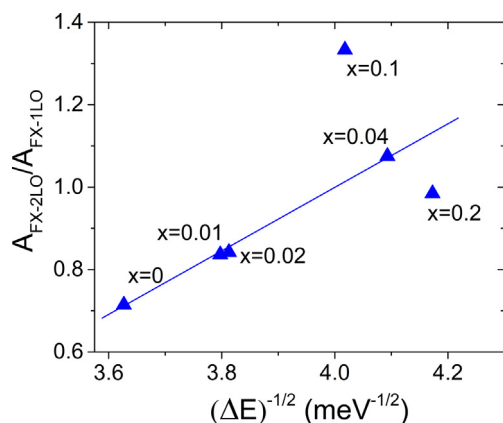

Fig. 13. The A_{FX-2LO}/A_{FX-1LO} ratio [from Fig. 12d] plotted against the energy difference ΔE [from Fig. 12c] to the power of −1/2. The solid line is a linear fit to the data for $Zn_{1-x}Ni_xO$ samples in the $0 \leq x \leq 0.04$ range.

crystallite sizes diminish again. The NiO phase is detected for x = 0.2.

(2) There is clear evidence for Ni diffusion towards the Si substrate during some stage or stages of the ZnNiO film fabrication process. A possible driving force for this effect, which seems to be more pronounced for higher x, is the very high diffusivity of Ni in Si.

(3) For low x values, Ni^{2+} partially substitutes Zn^{2+} in wurtzite $Zn_{1-x}Ni_xO$ lattice, as evidenced by a reduction of the lattice parameter by XRD, the observation of oxidized Ni by XPS and the absence of the NiO phase in the XRD patterns.

(4) The PL spectra evidence a preferential suppression of the defect-related emission in the visible with increasing nominal Ni content for $0.01 \leq x \leq 0.1$. For x = 0.2 the defect band becomes relatively large again.

(5) As in pure ZnO, the UV emission in ZnNiO is dominated by the first two phonon replica of the excitonic emission. The first and second replica blueshift by up to ~30 and ~15 meV, respectively, in consistency with a reduction of the LO phonon energy $\hbar\omega_{LO}$ by up to ~15 meV, for $Zn_{1-x}Ni_xO$ within the $0 \leq x \leq 0.04$ range. This reduction of $\hbar\omega_{LO}$ is shown to be correlated with the experimental increase of the exciton-phonon coupling, in consistency with the expected increase of the Fröhlich coupling constant for decreasing $\hbar\omega_{LO}$.

Acknowledgments

References

[1] K. Ellmer, Past achievements and future challenges in the development of optically transparent electrodes, Nat. Photon. 6 (2012) 809–817.
[2] M.R. Alenezi, S.J. Henley, S.R.P. Silva, On-chip fabrication of high performance nanostructured ZnO UV detectors, Sci. Rep. 5 (2015) 8516.
[3] S. Calnan, A.N. Tiwari, High mobility transparent conducting oxides for thin film solar cells, Thin Solid Films 518 (2010) 1839–1849.
[4] D.R. Miller, S.A. Akbar, P.A. Morris, Nanoscale metal oxide-based heterojunctions for gas sensing: a review, Sens. Actuators B Chem. 204 (2014) 250–272.
[5] O. Marin, G. Grinblat, A.M. Gennaro, M. Tirado, R.R. Koropecki, D. Comedi, On the origin of white photoluminescence from ZnO nanocones/porous silicon heterostructures at room temperature, Superlattices Microstruct. 79 (2015) 29–37.
[6] E. Mosquera, C. Rojas-Michea, M. Morel, F. Gracia, V. Fuenzalida, R.A. Zárate, Zinc oxide nanoparticles with incorporated silver: structural, morphological, optical and vibrational properties, Appl. Surf. Sci. 347 (2015) 561–568.
[7] E. Mosquera, I. Del Pozo, M. Morel, Structure and red shift of optical band gap in CdO-ZnO nanocomposite synthesized by the sol gel method, J. Solid State Chem. 206 (2013) 265–271.
[8] G. Srinet, R. Kumar, V. Sajal, Structural, optical, vibrational, and magnetic properties of sol-gel derived Ni doped ZnO nanoparticles, J. Appl. Phys. 114 (2013).
[9] C. Cheng, G. Xu, H. Zhang, Y. Luo, Hydrothermal synthesis Ni-doped ZnO nanorods

with room-temperature ferromagnetism, Mater. Lett. 62 (2008) 1617–1620.

[10] J.K. Salem, T.M. Hammad, R.R. Harrison, Synthesis, structural and optical properties of Ni-doped ZnO micro-spheres, J. Mater. Sci. Mater. Electron. 24 (2013) 1670–1676.

[11] D.C. Joshi, K. Dasari, S. Nayak, R. Palai, P. Suresh, S. Thota, Localized charge carrier transport properties of $Zn_{1-x}Ni_xO/NiO$ two-phase composites, J. Elec. Mater. 45 (2016) 2059.

[12] Y. Liu, T. Wang, X. Sun, Q. Fang, Q. Lv, X. Song, Z. Sun, Structural and photoluminescent properties of Ni doped ZnO nanorod arrays prepared by hydrothermal method, Appl. Surf. Sci. 257 (2011) 6540–6545.

[13] M. Zhong, Y. Li, M. Tariq, Y. Hu, W. Li, M. Zhu, H. Jin, Y. Li, Effect of oxygen vacancy induced by pulsed magnetic field on the room-temperature ferromagnetic Ni-doped ZnO synthesized by hydrothermal method, J. Alloys Compd. 675 (2016) 286–291.

[14] S.C. Das, R.J. Green, J. Podder, T.Z. Regier, G.S. Chang, A. Moewes, Band gap tuning in ZnO through Ni doping via spray pyrolysis, J. Phys. Chem. C 117 (2013) 12745–12753.

[15] D. Kouyate, J.C. Ronfard-Haret, P. Valat, J. Kossanyi, U. Mammel, D. Oelkrug, Quenching of zinc oxide photoluminescence by d- and f-transition metal ions, J. Lumin. 46 (1990) 326–337.

[16] M. Jlassi, I. Sta, M. Hajji, H. Ezzaouia, Effect of nickel doping on physical properties of zinc oxide thin films prepared by the spray pyrolysis method, Appl. Surf. Sci. 301 (2014) 216.

[17] Z. Yu, S. Ge, Y. Zuo, G. Wang, F. Zhang, Vacancy-induced room-temperature ferromagnetism in ZnO rods synthesized by Ni-doped solution and hydrothermal method, Appl. Surf. Sci. 256 (2010) 5813–5817.

[18] V. Jayaram, B. Sirisha, Rani, Soft chemical routes to the synthesis of extended solid solutions of wurtzite ZnO-MO (M = Mg Co, Ni), Mater. Sci. Eng. A 304–306 (2001) 800–804.

[19] S.K. Mandal, A.K. Das, T.K. Nath, D. Karmakar, Temperature dependence of solubility limits of transition metals (Co, Mn, Fe, and Ni) in ZnO nanoparticles, Appl. Phys. Lett. 89 (2006) 1–4.

[20] The integrated intensities obtained in the fitting of the experimental data where divided by the photoemission cross sections to make them proportional to the element concentrations. Taken from J.J. Yeh, I. Lindau, Atomic Subshell Photoionization Cross Sections and Asymmetry Parameters: 1 < Z < 103. Atomic Data and Nuclear Data Tables, 32 (1985) 1–155. Additionally, to ease the analysis, the vertical scales of figures 6 and 7 were chosen so that the normalized intensity of the O1s peak (first seven data points average) is one.

[21] M. Kumar, A. Kumar, A.C. Abhyankar, Influence of texture coefficient on surface morphology and sensing properties of W-doped nanocrystalline tin oxide thin films, ACS Appl. Mater. Interfaces 7 (2015) 3571–3580.

[22] L. Znaidi, Sol-gel-deposited ZnO thin films: a review, Mater. Sci. Eng. B Solid-State Mater. Adv. Technol. 174 (2010) 18–30.

[23] O. Marin, M. Tirado, N. Budini, E. Mosquera, C. Figueroa, D. Comedi, Photoluminescence from c-axis oriented ZnO films synthesized by sol-gel with

diethanolamine as chelating agent, Mater. Sci.Semicond. Process. 56 (2016) 59–65.

[24] J. Rodriguez-Carvajal, Recent advances in magnetic structure determination by neutron powder diffraction, Physica B 192 (1993) 55–69.

[25] N.C. Vega, O. Marin, E. Tosi, G. Grinblat, E. Mosquera, M.S. Moreno, M. Tirado, D. Comedi, The shell effect on the room temperature photoluminescence from ZnO/MgO core/shell nanowires: exciton-phonon coupling and strain, Nanotechnology 28 (2017) 275702.

[26] W. Shan, W. Walukiewicz, J.W. Ager, K.M. Yu, H.B. Yuan, H.P. Xin, G. Cantwell, J.J. Song, Nature of room-temperature photoluminescence in ZnO, Appl. Phys. Lett. 191911 (2005) 86–89.

[27] Nickel Diffusion and Configuration in Crystalline Zinc Oxide, Master Dissertation, Oslo University, 2014, available in: https://www.duo.uio.no/bitstream/handle/10852/40651/Thesis_Thomas_Sky.pdf?sequence=1.

[28] N. Yarykin, J. Weber, Evidence for room-temperature in-diffusion of nickel into silicon, Appl. Phys. Lett. 109 (2016) 102101.

[29] L.J. Chen, K.N. Tu, Epitaxial growth of transition-metal silicides on silicon, Mater Sci. Rep. 6 (1991) 53–140.

[30] S.T. Breviglieri, E.T.G. Cavalheiro, G.O. Chierice, Correlation between ionic radius and thermal decomposition of Fe (II), Co (II), Ni (II), Cu (II) and Zn (II) diethanoldithiocarbamates, Thermochim. Acta. 356 (2000) 79–84.

[31] T. Schuler, M.A. Aegerter, Optical, electrical and structural properties of sol gel ZnO: Al coatings, Thin Solid Films 351 (1999) 125–131.

[32] S.F. Chichibu, K. Kojima, Y. Yamazaki, K. Furusawa, A. Uedono, Controlling the carrier lifetime of nearly threading-dislocation-free ZnO homoepitaxial films by 3d transition-metal doping Controlling the carrier lifetime of nearly threading-dislocation-free ZnO homoepitaxial films by 3d transition-metal doping, Appl. Phys. Lett. 108 (2016) 21904.

[33] S. Mnasri, S. Abdi-Ben Nasrallah, N. Sfina, N. Bouarissa, M. Said, Electronic, lattice vibration and mechanical properties of CdTe, ZnTe, MnTe, MgTe, HgTe and their ternary alloys, Semicond. Sci. Technol. 24 (2009) 095008.

[34] C. Bundesmann, A. Rahm, M. Lorenz, M. Grundmann, M. Schubert, J. Appl. Phys. 99 (2006) 113504.

[35] C.-H. Ho, Y.-M. Kuop, C.-H. Chan, Y.-R. Ma, Optical characterization of strong UV luminescence emitted from the excitonic edge of nickel oxide nanotowers, Sci. Rep. 5 (2015) 15856.

[36] R.P. Wang, G. Xu, P. Jin, Size dependence of electron-phonon coupling in ZnO nanowires, Phys. Rev. B 69 (2004) 113303.

[37] GaAs and Related Materials: Bulk Semiconducting and Superlattice Properties, World Scientific, Singapore, 1994.

[38] T. Hanada, Basic properties of ZnO, GaN, and related materials, in: T. Yao, S.K. Hong (Eds.), Oxide and Nitride Semiconductors. Advances in Materials Research, Springer, Berlin, Heidelberg, 2009.

[39] P.J. Gielisse, J.N. Plendl, L.C. Mansur, R. Marshall, S.S. Mitra, R. Mykolojewicz, A. Smakula, Infrared properties of NiO and CoO and their mixed crystals, J. Appl. Phys. 36 (1965) 2446.